Multiple instabilities of thermocapillary flow in a cylindrical pool with a rotating disk on the free surface

Jinchao He,[1,2,3] Hao Liu,[1,2,3,*] Qiulin Li,[1,2,3] Na Zhang,[4] Mi Nie,[5] and Weina Mao[5]

[1]*Chongqing Southwest Research Institute for Water Transport Engineering, Chongqing Jiaotong University, Chongqing 400016, China*

[2]*Key Laboratory of Inland Waterway Regulation Engineering Ministry of Communications, Chongqing Jiaotong University, Chongqing 400074, China*

[3]*Chongqing Xike Consulting Center for Water Transport Engineering, Chongqing 400016, China*

[4]*Upper Changjiang River Bureau of Hydrological and Water Resources Survey, Chongqing 400020, China*

[5]*Chongqing Urban Construction Investment (Group) Co., Ltd., Chongqing 400015, China*

(Received 16 February 2022; accepted 17 April 2022; published 3 May 2022)

The thermocapillary flow instabilities of silicon melt in a cylindrical pool with a rotating disk on the free surface (a simplified model of the Czochralski crystal growth) are numerically investigated by using the linear stability analysis. The complete neutral or critical stability curves are determined. Results show that the neutral stability curves form a closed region in the parameter plane, in which the steady axisymmetric flow is linearly stable. Two types of rotating wave (RW1 and RW2) instabilities and two types of hydrothermal wave (HTW1 and HTW2) instabilities are found. The energy analysis shows that all the instabilities are hydrodynamic (inertial) in nature. Specifically, RW1 and RW2 are caused by the azimuthal shear induced by the crystal rotation, while HTW1 and HTW2 are caused by the radial shear induced by the thermocapillary force.

DOI: 10.1103/PhysRevE.105.055101

I. INTRODUCTION

Monocrystalline silicon has important applications in high-tech industries such as photovoltaic solar battery, chip, computer, and so on. In the semiconductor silicon industry, the Czochralski method is the most commonly used method for growing large-size monocrystalline silicon [1–3]. In fact, the Czochralski technique is the most important method for the production of electronic materials such as silicon, germanium, and different semiconducting compounds [4]. In the process of Czochralski crystal growth, the thermocapillary force, thermal buoyancy, and crystal rotation will drive a complex melt convection, and the instability of the melt convection has a serious impact on the quality of crystal growth [5–7]. The occurrence of flow instability may cause irregular patterns such as the spoke patterns [1,8], the reconstruction of the crystal chemical components, or stripes (microsegregation) [9], or even cause the spiral growth phenomena [2,3], resulting in the failure of crystal growth. Therefore, in the past few decades, many experimental [10–19] and numerical [20–30] works have been devoted to the study of flow instability in the Czochralski crystal growth.

Lee and Chun [11] experimentally studied the oscillatory convection induced by thermal buoyancy and crystal rotation in a Czochralski crucible. Thermal waves traveling in the azimuthal direction were observed when the rotation rate of crystal exceeded a certain threshold value, and the thermal waves disappeared when the rotation rate was large enough to suppress the thermal convection. Hintz and Schwabe [12,13] investigated the mixed convection driven by thermal buoyancy, thermocapillary force, and crystal rotation in a Czochralski crucible, and they found that the mixed convection was strongly influenced by the thermocapillary force. In addition, an oscillatory transition is observed when the rotation rate of crystal reaches a critical value, and this critical value increases linearly with the temperature difference. Kanda [14] experimentally studied the flow instability in a Czochralski crucible when the crystal and crucible rotate in the same direction under isothermal conditions. It is found that there are elliptical instability and circular shear instability in the forced convection with the increase of the difference between the crystal and crucible rotation rate. Teitel *et al.* [16] performed experiments to investigate the flow instability of large-Prandtl-number fluid in the Czochralski model, and pointed out that the increase of crystal radius and crystal rotation rate will destabilize the flow, while the increase of Prandtl number will stabilize the flow. Shen *et al.* [17,18] experimentally investigated the effects of aspect ratio and crystal and crucible rotation on the thermal convection stability in the Czochralski crucible, and indicated that the crystal rotation reduces the thermal convection stability when the aspect ratio is small, while the crystal rotation improves the thermal convection stability when the aspect ratio is large. Yu *et al.* [19] experimentally studied the flow instability of a binary mixture driven by rotation and thermal-solutal capillary force in a shallow Czochralski configuration. Their results show that the critical Marangoni number increases at first, then decreases with the increase of crystal rotation rate.

Compared with experimental research, the numerical simulation can reveal the details and evolution process of the flow instability. Zeng *et al.* [20,21] numerically found that the flow

*Corresponding author: liuh@cqjtu.edu.cn

structure and oscillation characteristics of melt convection in the Czochralski crucible were strongly affected by the crystal rotation rate. Based on the model of Zeng *et al.* [20,21], Gelfgat *et al.* [22,23] numerically studied the influence of crystal rotation on the instability of thermal convection by means of linear stability analysis, and found that as the crystal rotation rate increases, the critical temperature difference for the flow instability first decreases and then increases. Li *et al.* [24] simulated the forced convection driven by the rotation of the crystal and crucible under isothermal conditions, and reported that the flow is always stable when the crucible is rotated alone, and the crystal and crucible rotating in the same direction is more stable than the crystal and crucible rotating in the opposite direction. Wu *et al.* [25–27] performed a series of three-dimensional numerical simulations to study the effects of crystal and crucible rotation on the instabilities of thermocapillary convection and thermal capillary-buoyancy convection of silicon melt in the Czochralski configuration, and showed that with the increase of the crystal rotation rate, the stability first decreases and then increases when the crucible depth is small. However, when the crucible depth is large, the stability first increases and then decreases as the crystal rotation rate increases. Bessonov [28] numerically analyzed the effects of Prandtl number and crystal and crucible rotation on the instabilities of mixed convection in the Czochralski model. It was found that for large Prandtl number melts, the appropriate combination of crystal rotation and crucible rotation can improve the flow stability by more than ten times. Recently, Liu *et al.* [29,30] performed linear stability analysis to study the effects of crystal rotation and rotating magnetic field on the instability of thermocapillary flow in a Czochralski model, and pointed out that the rotating magnetic field can significantly improve the flow stability when the crystal and the magnetic field rotate in the same direction.

Although there has been a lot of research work on the flow instability in the Czochralski crucible, the research conclusions of different scholars are quite different, and some are even contradictory. For example, Hintz and Schwabe [12] pointed out that with the increase of crystal rotation rate, the critical temperature difference for the onset of flow instability in the Czochralski crucible increases, and the critical temperature difference is independent of crucible depth. However, Shen *et al.* [17,18] found that when the crucible depth is small, the crystal rotation reduces the critical temperature difference for the flow instability, while when the crucible is deep, the crystal rotation improves the critical temperature difference for the flow instability. The above discrepancies indicate that the current research still lacks a unified and deep understanding on the instability and corresponding mechanism of the complex convection in the Czochralski crucible. Therefore, it is still necessary to study in depth the instability of melt convection in the Czochralski crucible.

For the mixed convection driven by multiple driving forces, it is difficult to find all instability modes via experiments or three-dimensional numerical simulations, due to a large number of cases need to be dealt with under the combinations of multiple parameters. In comparison, the linear stability analysis can study flow instability more efficiently because it can transform the three-dimensional problems into two-dimensional or one-dimensional problems. The present paper aims to investigate the multiple instabilities of the mixed convection driven by the thermocapillary force and crystal rotation, and give the complete neutral or critical stability curves. For this purpose, the linear stability analysis is used to study the flow instability in the Czochralski crucible, and the energy analysis is employed to reveal the physical mechanism of the flow instability. This paper not only contains a summary of previous findings, but also reports some different results, and provides a helpful understanding for the flow instability driven by multiple drive forces.

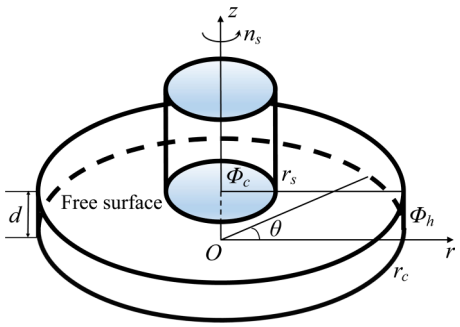

FIG. 1. Geometric and physical model of the Czochralski configuration.

II. MODELS AND METHODS

A. Physical and mathematical models

In the Czochralski process, an oriented single-crystal seed attached to a cooled pulling shaft is initially dipped into the melt contained in a heated cylindrical crucible. Then the single-crystal seed is slowly rotated and pulled up. In this way, a large oriented monocrystalline ingot is grown from its melt [4]. We consider a simplified model of the Czochralski crystal growth, as shown in Fig. 1. The crucible with depth d and radius r_c is filled with silicon melt, which is regarded as an incompressible Newtonian fluid of density ρ, kinematic viscosity ν, and thermal conductivity κ. The crystal with radius r_s rotates on the melt surface along the counterclockwise direction, which is defined as the positive azimuthal direction. The sidewall of crucible is maintained at a constant temperature Φ_h, the crystal-melt interface is maintained at the crystallization temperature Φ_c ($\Phi_h > \Phi_c$), and the bottom of crucible and the melt surface are considered as adiabatic. Because the capillary number is quite small, the free surface is assumed to be nondeformable and flat, and the surface tension σ of silicon melt varies with temperature Φ as $\sigma = \sigma_0 - \gamma_T \Phi$, where γ_T is the surface tension coefficient, and σ_0 is the surface tension at the reference temperature Φ_c. The gravity (buoyancy) is neglected since the crucible depth is small. In addition, the no-slip condition is imposed to all solid-liquid boundaries, and the melt convection is considered as laminar flow.

All variables are made dimensionless using the crucible radius r_c as the length scale, therefore the geometry of the convective system can be determined by the aspect ratio $\varepsilon = d/r_c$ and the radius ratio $\beta = r_s/r_c$. In this study, the aspect ratio and radius ratio are fixed at $\varepsilon = 0.06$ and $\beta = 0.3$, respectively. The time t velocity $\boldsymbol{u} = (u, v, w)$ and the pressure p are scaled with r_c^2/ν, ν/r_c, and $\rho\nu^2/r_c^2$,

respectively, where u, v, and w are the velocity components in the radial, azimuthal, and axial directions of the cylindrical coordinates. The dimensionless temperature T is defined as $T = (\Phi - \Phi_c)/(\Phi_h - \Phi_c)$. Then the dimensionless governing equations in the cylindrical coordinates are

$$\nabla \cdot \boldsymbol{u} = 0 \tag{1}$$

$$\frac{\partial \boldsymbol{u}}{\partial t} + (\boldsymbol{u} \cdot \nabla)\boldsymbol{u} = -\nabla p + \nabla^2 \boldsymbol{u} \tag{2}$$

$$\frac{\partial T}{\partial t} + (\boldsymbol{u} \cdot \nabla)T = \frac{1}{\mathrm{Pr}}\nabla^2 T \tag{3}$$

Here the dimensionless parameter $\mathrm{Pr} = \nu/\kappa$ is the Prandtl number, and the Prandtl number of silicon melt is $\mathrm{Pr} = 0.011$ [31].

The dimensionless boundary conditions are as follows: the free surface ($z = \varepsilon$, $\beta < r < 1$),

$$\frac{\partial u}{\partial z} = -\frac{\mathrm{Ma}}{\mathrm{Pr}}\frac{\partial T}{\partial r}, \quad \frac{\partial v}{\partial z} = -\frac{\mathrm{Ma}}{\mathrm{Pr}}\frac{\partial T}{r\partial \theta}, \quad w = 0, \frac{\partial T}{\partial z} = 0, \tag{4}$$

the melt-crystal interface ($z = \varepsilon$, $0 \leqslant r \leqslant \beta$),

$$u = w = 0, v = \frac{\mathrm{Re}}{\beta} r, T = 0, \tag{5}$$

the bottom ($z = 0$, $0 \leqslant r < 1$),

$$u = v = w = 0, \frac{\partial T}{\partial z} = 0, \tag{6}$$

and the crucible sidewall ($r = 1$, $0 \leqslant z \leqslant \varepsilon$),

$$u = v = w = 0, T = 1. \tag{7}$$

Here the dimensionless parameters, $\mathrm{Ma} = \gamma_T r_c(\Phi_h - \Phi_c)/(\rho\nu\kappa)$ and $\mathrm{Re} = (2\pi n_s r_s r_c)/(60\nu)$, are the Marangoni number and the rotation Reynolds number, respectively, where n_s (rpm) is the rotation rate of the crystal.

B. Basic flow and linear stability analysis

The system of Eqs. (1)–(7) admits an axisymmetric steady-state solution, called the basic flow. The basic flow is first simulated by the spectral element method [30,32]. The linear stability of the basic flow can be analyzed by adding the infinitesimal disturbances to the basic flow:

$$(\boldsymbol{u}, p, T) = (\boldsymbol{u}_0, p_0, T_0) + (\hat{u}, \hat{p}, \hat{T}). \tag{8}$$

Here $(\boldsymbol{u}_0, p_0, T_0)$ is the basic flow, and $(\hat{u}, \hat{p}, \hat{T})$ is the infinitesimal disturbance. Then the linearized disturbance equations and corresponding boundary conditions are obtained by substituting Eq. (8) into Eqs. (1)–(7) and discarding the second-order infinitesimal and the basic-state part:

$$\nabla \cdot \hat{u} = 0, \tag{9}$$

$$\frac{\partial \hat{u}}{\partial t} + (\boldsymbol{u}_0 \cdot \nabla)\hat{u} + (\hat{u} \cdot \nabla)\boldsymbol{u}_0 = -\nabla \hat{p} + \nabla^2 \hat{u}, \tag{10}$$

$$\frac{\partial \hat{T}}{\partial t} + (\boldsymbol{u}_0 \cdot \nabla)\hat{T} + (\hat{u} \cdot \nabla)T_0 = \frac{1}{\mathrm{Pr}}\nabla^2 \hat{T}, \tag{11}$$

the free surface ($z = \varepsilon$, $\beta < r < 1$),

$$\frac{\partial \hat{u}}{\partial z} = -\frac{\mathrm{Ma}}{\mathrm{Pr}}\frac{\partial \hat{T}}{\partial r}, \quad \frac{\partial \hat{v}}{\partial z} = -\frac{\mathrm{Ma}}{\mathrm{Pr}}\frac{\partial \hat{T}}{r\partial \theta}, \quad \hat{w} = 0, \frac{\partial \hat{T}}{\partial z} = 0, \tag{12}$$

the melt-crystal interface ($z = \varepsilon$, $0 \leqslant r \leqslant \beta$),

$$\hat{u} = \hat{v} = \hat{w} = 0, \hat{T} = 0, \tag{13}$$

the bottom ($z = 0$, $0 \leqslant r < 1$),

$$\hat{u} = \hat{v} = \hat{w} = 0, \frac{\partial \hat{T}}{\partial z} = 0, \tag{14}$$

and the crucible sidewall ($r = 1$, $0 \leqslant z \leqslant \varepsilon$),

$$\hat{u} = \hat{v} = \hat{w} = 0, \hat{T} = 0. \tag{15}$$

The general solution of Eqs. (9)–(15) can be written as an infinite sum of normal modes in the form

$$\begin{pmatrix} \hat{u} \\ \hat{p} \\ \hat{T} \end{pmatrix}(r, \theta, z, t) = \begin{pmatrix} \tilde{u} \\ \tilde{p} \\ \tilde{T} \end{pmatrix}(r, z) e^{(\tau + i\omega)t + im\theta}. \tag{16}$$

Here m is the wave number in the azimuthal direction of the normal mode, τ is its real growth rate, and ω is its oscillation frequency. By using the spectral element method for spatial discretization, the linear system of Eqs. (9)–(15) can be written in a generalized eigenvalue problem:

$$\boldsymbol{A}\tilde{x} = (\tau + i\omega)\boldsymbol{B}\tilde{x}. \tag{17}$$

For linear stability analysis the leading eigenvalue $(\tau + i\omega)$ has been solved using the Arnoldi algorithm from the ARPACK library [33]. To determine the neutral stability curves, we must find the Marangoni numbers and rotation Reynolds numbers at which the growth rate τ of the leading eigenvalue is equal to zero. The critical stability curves are the lower envelope curves of the neutral stability curves. For a determined neutral mode or critical mode, the corresponding frequency ω indicates the oscillation state. Moreover, the propagation angular velocity of the oscillating wave is defined as $\eta = -\omega/m$. Therefore, $\omega < 0$ and $\omega > 0$ indicate that the oscillating wave propagate in the counterclockwise and clockwise direction, respectively.

C. Energy analysis

Once the linear stability problem is solved, it is useful to compute the energy-transfer rates from the basic flow to the neutral or critical disturbance mode. The contribution and the spatial distribution of the local energy can provide physical insight into the instability mechanism. In addition, the calculation of disturbance energy is *a posteriori* examination of the linear stability results, since the production of disturbance energy should be balanced by the viscous dissipation at any neutral or critical modes. The disturbance kinetic energy (E_{kin}) is defined as

$$E_{\mathrm{kin}} = \frac{1}{2}\int_V \hat{u} \cdot \hat{u} dV. \tag{18}$$

Therefore, the change rate of disturbance kinetic energy can be expressed as

$$\frac{\partial E_{\rm kin}}{\partial t} = \frac{\partial\left(\frac{1}{2}\int_V \hat{u}\cdot\hat{u}dV\right)}{\partial t} = \int_V \hat{u}\cdot\frac{\partial\hat{u}}{\partial t}dV. \tag{19}$$

Substituting the disturbance equation Eq. (10) into Eq. (19) and using some algebra, the change rate of the disturbance kinetic energy can be derived as [34,35]

$$\frac{1}{D_k}\frac{\partial E_{\rm kin}}{\partial t} = I_v + M - 1 \tag{20}$$

which has been normalized by the viscous dissipation rate of kinetic energy D_k,

$$D_k = \int_V (\nabla\times\hat{u})^2 dV. \tag{21}$$

I_v is the energy-transfer rate from the basic flow to the disturbances, and M is the rate of work done by Marangoni stress on the free surface. The expressions of the above energy terms are

$$\begin{aligned} I_v &= I_{v1}+I_{v2}+I_{v3}+I_{v4}+I_{v5}+I_{v6}+I_{v7}+I_{v8} \\ &= \frac{1}{D_k}\int_V\left(-\hat{u}\hat{u}\frac{\partial u_0}{\partial r} - \hat{u}\hat{w}\frac{\partial u_0}{\partial z} + \frac{\hat{u}\hat{v}v_0}{r} - \hat{u}\hat{v}\frac{\partial v_0}{\partial r}\right. \\ &\quad \left. -\hat{v}\hat{w}\frac{\partial v_0}{\partial z} - \frac{\hat{v}\hat{v}u_0}{r} - \hat{u}\hat{w}\frac{\partial w_0}{\partial r} - \hat{w}\hat{w}\frac{\partial w_0}{\partial z}\right)dV, \end{aligned} \tag{22}$$

$$M = \frac{1}{D_k}\int_S\left(\hat{u}\frac{\partial\hat{u}}{\partial z}+\hat{v}\frac{\partial\hat{v}}{\partial z}\right)dS. \tag{23}$$

The positive value of the above energy term indicates that it promotes the flow instability, and the negative value indicates that it has a stabilizing effect.

III. NUMERICAL RESULTS AND DISCUSSION

All numerical codes are based on the spectral-element discretization and have been verified in our previous articles [30,32]. The present results are computed using a nonuniform grid with $N_r \times N_z = 155 \times 26$ points in the radial and axial directions, respectively. In order to check the grid convergence, the growth rate τ and the frequency ω corresponding to the real and the imaginary parts of the leading eigenvalue are plotted in Fig. 2 as functions of the wave number m for Re = 2400 and Ma = 1155. It can be seen from Fig. 2 that the results obtained from the selected grid ($N_r \times N_z = 155 \times 26$) are consistent with those obtained from a finer grid ($N_r \times N_z = 166 \times 31$).

A. Basic flow

When the Marangoni number and the rotation Reynolds number are small, the melt convection is steady and axisymmetric, called the basic flow. Figure 3 shows the representative structures of the basic flow. When the crystal rotation is absent, the inward thermocapillary force induces a counterclockwise main vortex below the free surface, and a secondary vortex is embedded into the main vortex near the crystal [Fig. 3(a)]. When the crystal rotation acts alone, the rotation drives a clockwise vortex cell under the crystal due to the outward centrifugal force [Fig. 3(b)]. When the crystal rotation and thermocapillary forces act together, these two driving forces will compete with each other, so that the two vortices in opposite directions interact [Figs. 3(c)–3(f)]. With the increase of Marangoni number, the main vortex induced by the thermocapillary force is strengthened, while the clockwise vortex caused by the crystal rotation is weakened.

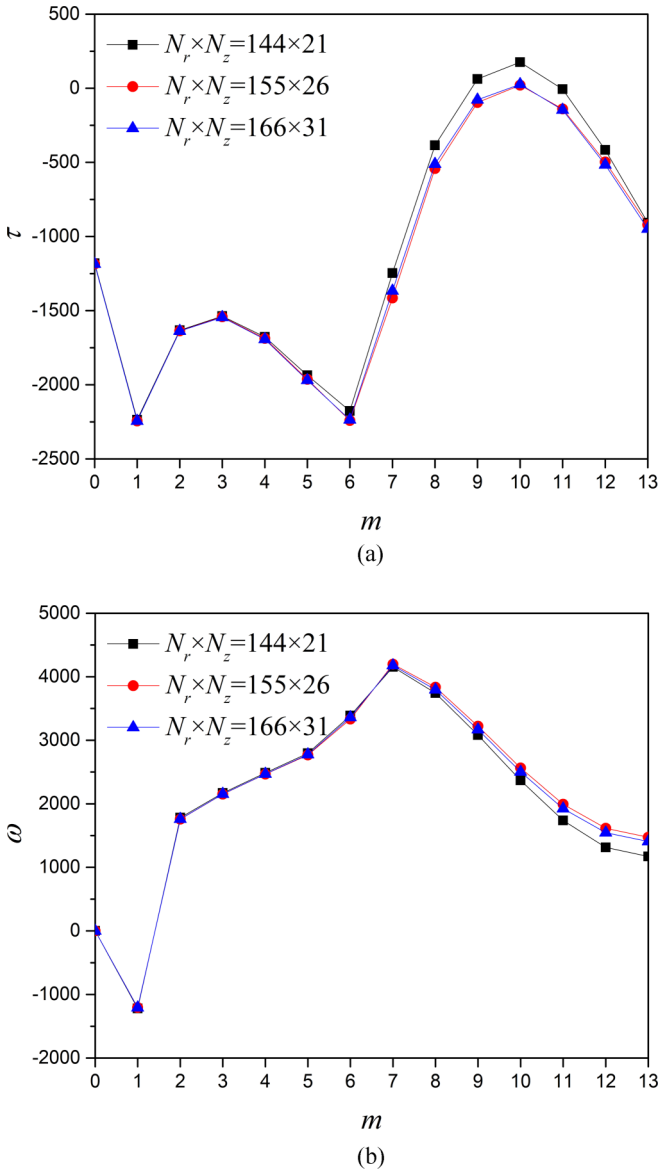

FIG. 2. (a) Growth rate τ and (b) frequency ω of the leading eigenvalue as functions of the wave number m for Re = 2400 and Ma = 1155.

B. Neutral and critical curves for the onset of flow instability

The steady and axisymmetric basic flow will lose its stability to become an oscillatory flow when the Marangoni number or the rotation Reynolds number exceeds a certain threshold value. When there is only the thermocapillary force, the flow instability occurs at about Ma = 1717. If there is only the crystal rotation, the basic flow will be unstable when the rotation Reynolds number exceeds Re = 1179. Figure 4 shows

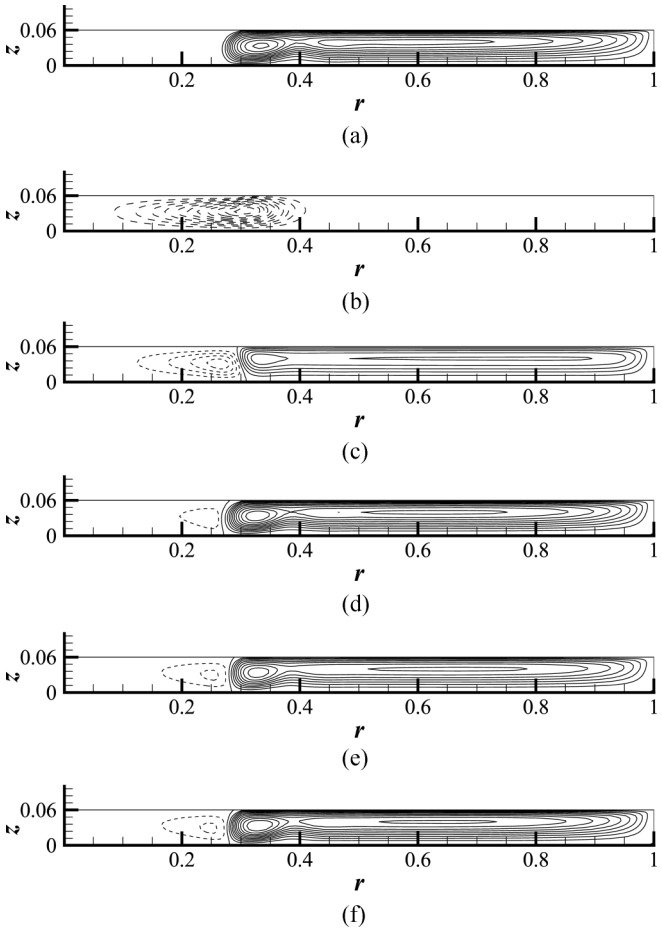

FIG. 3. Streamlines of the basic flow (dashed lines correspond to negative values). (a) Re = 0, Ma = 1760; (b) Re = 1180, Ma = 0; (c) Re = 1800, Ma = 116; (d) Re = 1800, Ma = 1113; (e) Re = 4200, Ma = 857; (f) Re = 4200, Ma = 1088.

the neutral or critical stability curves in the parameter (Re-Ma) plane. Four types of flow instabilities (two types of rotating waves, denoted as RW1 and RW2, and two types of hydrothermal waves, denoted as HTW1, HTW2) are predicted by the linear stability analysis results. The horizontal axis, vertical axis, and the four neutral stability curves form a closed parameter region, in which the basic flow is linearly stable. In particular, in the interval $1179 < \mathrm{Re} < 4593$, the flow state will undergo two transitions from unstable to stable, and then from stable to unstable with the increase of Marangoni number. For $\mathrm{Re} > 4593$, the basic flow is always linearly unstable. Figure 5 shows the propagation angular velocity η of the four types of oscillatory flow as a function of the rotation Reynolds number Re. With the increase of Re, the propagation angular velocity of HTW1 decreases, while the propagation angular velocity of HTW2, RW1, and RW2 increases almost linearly. The detailed neutral or critical instability values are listed in Table I.

C. Instability type and mechanism

1. Instability mechanism of RW1

When the Marangoni number is relatively small ($\mathrm{Ma} < 262$), the RW1 occurs if the rotation Reynolds number exceeds a critical value. With the increase of

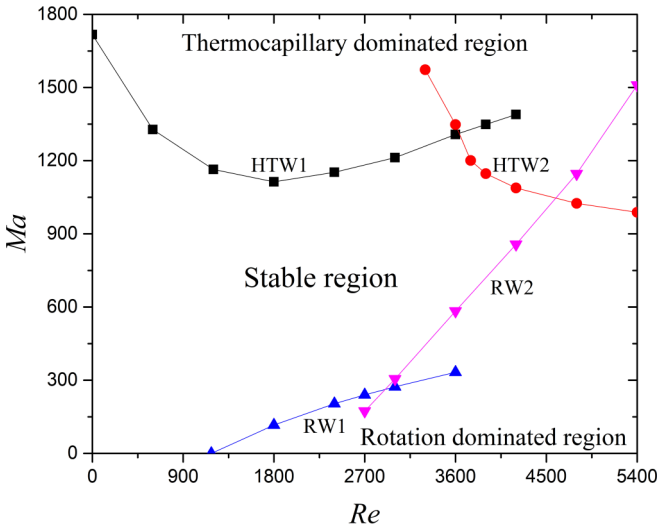

FIG. 4. Neutral or critical stability curves in the Re-Ma plane.

Marangoni number, this critical value increases almost linearly. Figure 6(a) shows the surface patterns of temperature disturbance for RW1, which are characterized by petal-like temperature fluctuations. For RW1 the wave number is always $m = 3$ and the rotating wave propagates in the counterclockwise direction, the same as the direction of crystal rotation. Moreover, the propagation angular velocity η of RW1 increases almost linearly with the increase of rotation Reynolds number (see Fig. 5).

Under the critical stability condition, the kinetic energy budgets for the incipience of flow instabilities are shown in Fig. 7. We can see from Fig. 7 that the Marangoni effect hardly contributes to the disturbance energy, indicating that the instabilities are hydrodynamic (inertial) in nature. For RW1, I_{v4} occupies a dominant position in the energy balance. $I_{v4} = -\int_V (\hat{u}\hat{v}\partial v_0/\partial r)dV/D_k$ measures the transfer of azimuthal basic-state momentum v_0 to the azimuthal disturbance $\hat{v}$ via the radial disturbance $\hat{u}$. Therefore, the instability

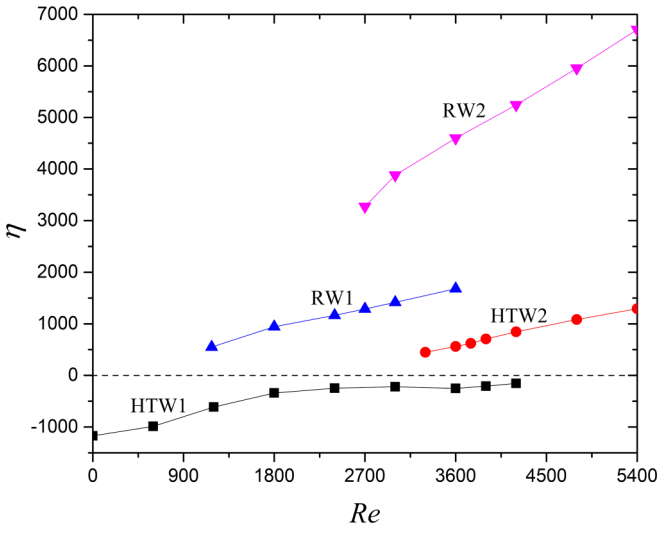

FIG. 5. Propagation angular velocity η of the oscillating waves as a function of the rotation Reynolds number Re.

TABLE I. Neutral or critical instability parameters and instability types.

Re	Ma_c (or Ma_n)	η	m	Type
1179	0	549.3	3	
1800	116	942.9	3	
2400	204	1164.4	3	RW1
2700	240	1287.7	3	
3000	273	1414.9	3	
3600	332	1679.4	3	
2700	173	3272.3	9	
3000	305	3881.2	11	
3600	583	4596.8	12	RW2
4200	857	5242.0	12	
4800	1146	5952.5	11	
5400	1510	6704.4	11	
0	1717	±1171.1	18	
600	1327	−987.5	11	
1200	1164	−612.0	11	
1800	1113	−339.7	11	HTW1
2400	1152	−247.8	10	
3000	1212	−220.6	9	
3600	1307	−251.3	8	
3300	1573	448.7	12	
3600	1348	562.3	12	
3750	1201	621.4	11	
3900	1147	705.3	11	HTW2
4200	1088	845.5	11	
4800	1025	1083.5	11	
5400	988	1292.0	11	

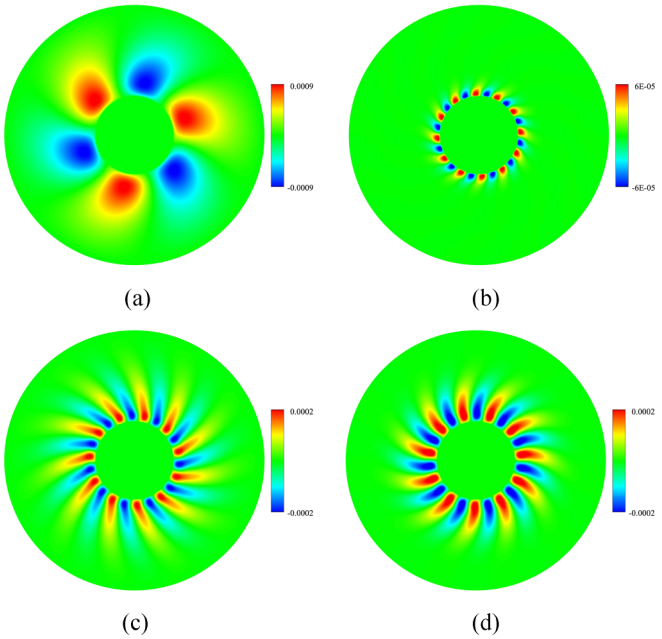

FIG. 6. Surface patterns of temperature disturbance for the four types of flow instabilities. (a) RW1, Re = 1800, Ma = 116; (b) RW2, Re = 4200, Ma = 857; (c) HTW1, Re = 1800, Ma = 1113; (d) HTW2, Re = 4200, Ma = 1088.

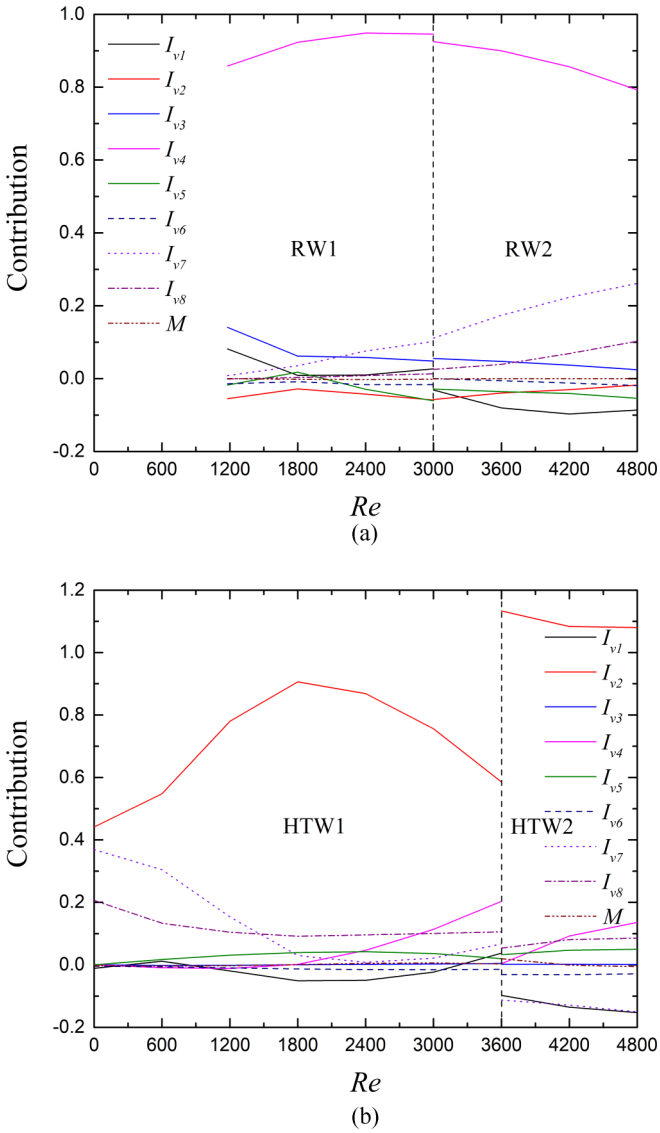

FIG. 7. Kinetic energy budget under the critical conditions. (a) For RW1 and RW2; (b) for HTW1 and HTW2.

of RW1 is caused by the azimuthal shear of basic flow induced by the crystal rotation.

2. Instability mechanism of RW2

For 262 < Ma < 1046, the RW2 becomes the critical mode when the rotation Reynolds number exceeds a critical value. This critical value increases linearly with the increase of Marangoni number, but the gradient is less than that of RW1. The surface patterns of RW2 are characterized by a series of small temperature spots distributed at the edge of the crystal. The amplitude of temperature fluctuation of RW2 is much smaller than that of RW1, but the phase velocity η of RW2 is larger than that of RW1. The propagation direction of RW2 is also counterclockwise, which is consistent with the crystal rotation. The kinetic energy budget [see Fig. 7(a)] shows that I_{v4} still plays a leading role in the energy balance. However, I_{v7}, representing the axial shear, also occupies a considerable proportion, and it increases as Re increases. In

general, instability of RW2 is still mainly caused by the azimuthal shear of the basic flow driven by the crystal rotation.

3. Instability mechanism of HTW1 and HTW2

The HTW1 arises as the most dangerous mode for relatively small rotation Reynolds number ($\mathrm{Re} < 3636$) and relatively large Marangoni number, and the HTW2 replaces it as the critical mode for larger rotation Reynolds number ($\mathrm{Re} > 3636$). With the increase of rotation Reynolds number, the critical Marangoni number for the onset of HTW1 instability decreases at first and then increases, and the critical Marangoni number for HTW2 instability decreases monotonously. The surface patterns of temperature disturbance for HTW1 and HTW2 are characterized by the curved spokelike temperature fluctuation [see Figs. 6(c) and 6(d)], and the amplitudes of fluctuation are between those of RW1 and RW2. The energy budgets under the critical conditions [see Fig. 7(b)] show that I_{v2} is the main source of disturbance energy for both HTW1 and HTW2. $I_{v2} = -\int_V (\hat{u}\hat{w}\partial u_0/\partial z)dV/D_k$ measures the transfer of radial basic-state momentum u_0 to the radial disturbance $\hat{u}$ via the axial disturbance $\hat{w}$. Therefore, instabilities of HTW1 and HTW2 are mainly caused by the radial shear of the basic flow, which is induced by the thermocapillary force. It should be noted that although the instabilities are mainly caused by the thermocapillary force, the contribution of Marangoni effect on the disturbance energy is almost zero [see Fig. 7(b)]. The perturbation flow field is only driven by the basic flow (inertial instability), and the perturbation temperature field is enslaved to the perturbation flow field.

The characteristics and mechanisms of HTW1 and HTW2 instabilities have been reported in our previous article [32], and the HTW1 is also reported by Wu *et al.* [25] in their three-dimensional numerical simulations. Moreover, the HTW1 and HTW2 instabilities are very similar to the hydrothermal waves in small-Prandtl-number fluid in the annular pool [36], and also similar to the spoke patterns in oxide melt in the Czochralski system [37].

IV. DISCUSSION

For the flow instability in the Czochralski crucible, the past research work mainly focused on the thermal convection instability and the effect of crystal rotation on the thermal convection instability. However, even for isothermal fluids, flow instability will still occur when the rotation rate of crystal exceeds a certain threshold, and this type of flow instability is often ignored. Wu *et al* [25]. studied the effect of crystal rotation on thermocapillary flow instability by three-dimensional numerical simulations, and they indicated that the critical Marangoni number decreases at first and then increases with the increase of rotation rate. In addition, the propagation direction of oscillatory flow is opposite to the direction of crystal rotation. Through comparative analysis with the present results, the instability they found belongs to HTW1. Shen *et al.* [17] experimentally found that the crystal rotation destabilizes the thermocapillary flow, and the propagation direction of oscillatory flow is consistent with the crystal rotation. The instability they found may belong to HTW2. Hintz and Schwabe [12] experimentally showed that the oscillatory instability occurs when the rotation rate of crystal exceeds some threshold value, and this threshold value is found to increase linearly with the temperature difference (Marangoni number) between the crucible and the crystal. It can be inferred that this instability belongs to RW1.

In fact, when the flow is driven by two or more driving forces, there may be multiple instabilities in the bifurcation diagram, owing to the competition and suppression among the different driving forces. For example, Yin *et al.* [31] investigated the thermocapillary flow instability in a rotating annular pool, they found that within a certain intermediate range of rotation rate, the flow state will undergo three transitions between stable and unstable as the Marangoni number increases, and a similar phenomenon was also reported by Li *et al.* [35] in the study of instabilities of thermocapillary-buoyant-Coriolis flow.

V. CONCLUSIONS

In this paper, a series of linear stability analyses based on the spectral element method are performed to understand the instability behavior of melt convection driven by thermocapillary force and crystal rotation in a Czochralski crucible. Four neutral or critical stability curves, representing four types of flow instabilities (HTW1, HTW2, RW1, and RW2), are predicted. The results show that the four neutral or critical stability curves enclose a closed region in the parameter (Re-Ma) plane, in which the steady and axisymmetric basic flow is linearly stable. The critical Marangoni number for the onset of HTW1 and HTW2 instabilities shows a downward trend in general with the increase of rotation Reynolds number, i.e., the crystal rotation destabilizes the thermocapillary flow. Contrarily, the critical rotation Reynolds number for the onset of RW1 and RW2 instabilities increases linearly as Marangoni number increases. In other words, the thermocapillary force stabilizes the forced convection driven by the crystal rotation. In particular, in the range $1179 < \mathrm{Re} < 4593$, the flow state will change twice with the increase of Marangoni number, due to the competition and suppression between the thermocapillary force and crystal rotation. The HTW1 is found to propagate in the opposite direction of crystal rotation, and the propagation angular velocity decreases with the increase of crystal rotation rate. Contrarily, HTW2, RW1, and RW2 propagate in the same direction as the crystal rotation, and the propagation angular velocity increases linearly with the increase of crystal rotation rate. The disturbance energy budgets under the neutral or critical conditions indicate that all the instabilities are triggered by the shear instability mechanism. For HTW1 and HTW2, the radial shear induced by the thermocapillary force is responsible for the flow instabilities, however the azimuthal shear induced by the crystal rotation is the main cause for the instabilities of RW1 and RW2.

The data that support the findings of this study are available from the corresponding author upon reasonable request.

ACKNOWLEDGMENTS

This work was supported by the Science and Technology Research Program of Chongqing Municipal Education Commission (Grant No. KJQN202100706), and the National Key R & D Plan (Grant No. 2018YFC1508602).

The authors have no conflicts to disclose.

[1] T. Azami, S. Nakamura, M. Eguchi, and T. Hibiya, J. Cryst. Growth **233**, 99 (2001).

[2] R. Uecker, H. Wilke, D. Schlom, B. Velickov, P. Reiche, A. Polity, M. Bernhagen, and M. Rossberg, J. Cryst. Growth **295**, 84 (2006).

[3] N. Crnogorac, H. Wilke, K. Cliffe, A. Y. Gelfgat, and E. Kit, Cryst. Res. Technol. **43**, 606 (2008).

[4] R. Fornari, in *Comprehensive Semiconductor Science and Technology*, edited by P. Bhattacharya, R. Fornari, and H. Kamimura (Elsevier, Amsterdam, 2011), p. 1.

[5] L. Davoust, J.-L. Achard, and L. Drazek, Phys. Rev. E **91**, 023019 (2015).

[6] H. Liu, J. He, Z. Zeng, and Z. Qiu, Phys. Rev. E **104**, 035101 (2021).

[7] R. Touihri, A. El Gallaf, D. Henry, and H. B. Hadid, Phys. Rev. E **84**, 056302 (2011).

[8] K. W. Yi, K. Kakimoto, M. Eguchi, M. Watanabe, T. Shyo, and T. Hibiya, J. Cryst. Growth **144**, 20 (1994).

[9] M. Jurisch, J. Cryst. Growth **102**, 223 (1990).

[10] H. Ozoe, K. Toh, and T. Inoue, J. Cryst. Growth **110**, 472 (1991).

[11] Y.-S. Lee and C.-H. Chun, Adv. Space Res. **24**, 1403 (1999).

[12] P. Hintz and D. Schwabe, J. Cryst. Growth **222**, 356 (2001).

[13] P. Hintz, D. Schwabe, and H. Wilke, J. Cryst. Growth **222**, 343 (2001).

[14] I. Kanda, Phys. Fluids **16**, 3325 (2004).

[15] S.-S. Son, P.-O. Nam, and K.-W. Yi, J. Cryst. Growth **292**, 272 (2006).

[16] M. Teitel, D. Schwabe, and A. Y. Gelfgat, J. Cryst. Growth **310**, 1343 (2008).

[17] T. Shen, C.-M. Wu, and Y.-R. Li, Int. J. Therm. Sci. **104**, 20 (2016).

[18] T. Shen, C.-M. Wu, L. Zhang, and Y.-R. Li, J. Cryst. Growth **438**, 55 (2016).

[19] J.-J. Yu, Y.-R. Li, L. Zhang, S. Ye, and C.-M. Wu, Int. J. Therm. Sci. **118**, 236 (2017).

[20] Z. Zeng, J. Chen, H. Mizuseki, K. Shimamura, T. Fukuda, and Y. Kawazoe, J. Cryst. Growth **252**, 538 (2003).

[21] Z. Zeng, J. Chen, H. Mizuseki, T. Fukuda, and Y. Kawazoe, J. Cryst. Growth **266**, 81 (2004).

[22] A. Y. Gelfgat, A. Rubinov, P. Bar-Yoseph, and A. Solan, J. Cryst. Growth **275**, e7 (2005).

[23] A. Y. Gelfgat, J. Cryst. Growth **303**, 226 (2007).

[24] Y.-R. Li, C.-M. Wu, S.-Y. Wu, and L. Peng, Phys. Fluids **21**, 084102 (2009).

[25] C.-M. Wu, Y.-R. Li, and R.-J. Liao, Int. J. Heat Mass Transfer **79**, 968 (2014).

[26] C.-M. Wu, Y.-R. Li, and R.-J. Liao, Phys. Fluids **26**, 104105 (2014).

[27] C.-M. Wu, D.-F. Ruan, Y.-R. Li, and R.-J. Liao, Int. J. Therm. Sci. **86**, 394 (2014).

[28] O. Bessonov, Fluid Dyn. **52**, 375 (2017).

[29] H. Liu, Z. Zeng, Z. Qiu, L. Yin, and Y. Xiao, Phys. Fluids **32**, 104106 (2020).

[30] Y. Liu, Z. Zeng, L. Zhang, H. Liu, Y. Xiao, and Y. Wang, Phys. Fluids **33**, 104101 (2021).

[31] L. M. Yin, Z. Zeng, Z. H. Qiu, H. Mei, L. Q. Zhang, and Y. X. Zhang, Int. J. Heat Mass Transfer **97**, 353 (2016).

[32] H. Liu, Z. Zeng, L. Yin, Z. Qiu, and L. Qiao, Int. J. Therm. Sci. **137**, 500 (2019).

[33] R. B. Lehoucq, D. C. Sorensen, and C. Yang, *ARPACK User's Guide: Solution of Large-scale Eigenvalue Problems with Implicitly Restarted Arnoldi Methods* (Siam, Philadelphia, 1998), Vol. 6.

[34] C. Nienhüser and H. C. Kuhlmann, J. Fluid Mech. **458**, 35 (2002).

[35] H.-M. Li, L. Feng, W.-Y. Shi, and M. K. Ermakov, Int. Commun. Heat Mass **130**, 105801 (2022).

[36] M. Lappa, Cryst. Res. Technol. **40**, 531 (2005).

[37] T. Tsukada, in *Handbook of Crystal Growth* (Elsevier, Amsterdam, 2015), p. 871.